Electronic Supplementary Material (ESI) for Journal of Materials Chemistry A.

Supplementary Information

Plasmonic Au nanoclusters dispersed in nitrogen-doped graphene as a robust photocatalyst for light-to-hydrogen conversion

Dung Van Dao,[†a] Luis A. Cipriano,[†b] Giovanni Di Liberto,[b] Thuy T.D. Nguyen,[c] Sang-Woo Ki,[d] Hoki Son,[a] Gyu-Cheol Kim,[a] Kang-Hyun Lee,[e] Jin-Kyu Jang,[d] Yeon-Tae Yu,[c] Gianfranco Pacchioni*[b] and In-Hwan Lee*[a]

Characterizations

The prepared photocatalysts were morphologically observed using transmission electron microscopy (TEM) with a JEM-2010 microscope (JEOL) operated at 200 kV. The crystalline structures were measured using an X-ray diffraction (XRD) system (D/Max 2005, Rigaku) and Cu Kα radiation (λ = 1.54178 Å). The optical properties were analyzed via UV–visible (UV–vis) spectroscopy with an Agilent/HP 8453 spectrophotometer at room temperature. XPS was conducted with a Multilab 2000 instrument (Thermo Fisher Scientific) and monochromated Al Kα radiation (hν = 1,486.6 eV) to study the surface chemical states of the elements present in the photocatalysts. The calibration was based on the binding energies of the resultant C 1s peak at approximately 285 eV. Spectral fitting was done using Casa XPS analysis software. The samples were deposited on conductive Si substrates for XPS measurement. The specific surface areas of the samples were estimated via the nitrogen gas adsorption method to generate high-quality data through the BET technique with a Micromeritics Tristar 3000 analyzer. The loading of Au nanostructures in N-Gr support was measured by inductively coupled plasma (ICP) spectrometry (ICPS-7500, Shimadzu) after the samples were treated with aqua regia at 100°C for 10 h. Raman spectra of samples was measured by a LabRam ARAMIS IR2 spectrometer. The height of graphene-based nanomaterials was determined by the atomic force microscope (AFM; Park System, XE-100).

Fig. S1 High-resolution TEM observation of free graphene

Fig. S1 describes the high-resolution TEM image of as-pyrolyzed free graphene with a uniform and multilayered morphologies. The wrinkles of graphene nanostructures are observed in each basic unit with overall sizes up to tens of micrometers.

(a)

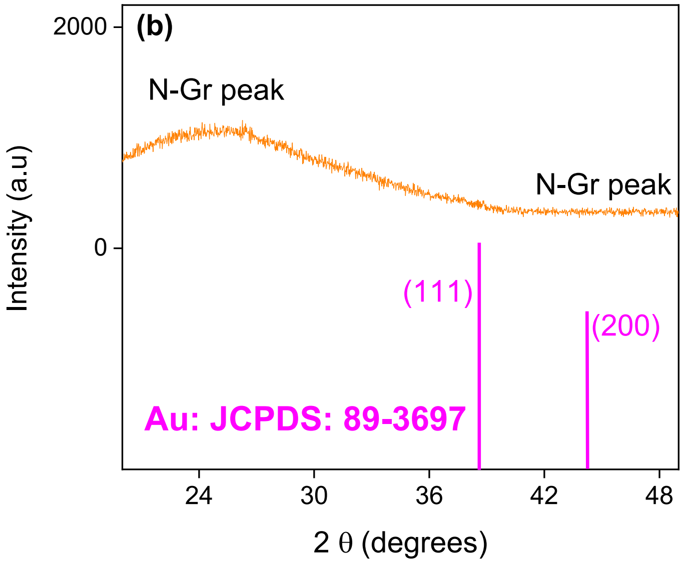

Fig. S2 (a) High-resolution TEM observation and (b) XRD pattern measurement of Au SAs/N-Gr nanocomposites.

Fig. S2a indicates Au SAs (as indicated by the yellow circles) dispersed in N-Gr support with the range sizes of 0.2 to 0.5 nm.

Fig. S2b presents the XRD measurement of Au SAs/N-Gr, at which the peaks of Au cannot be detected.

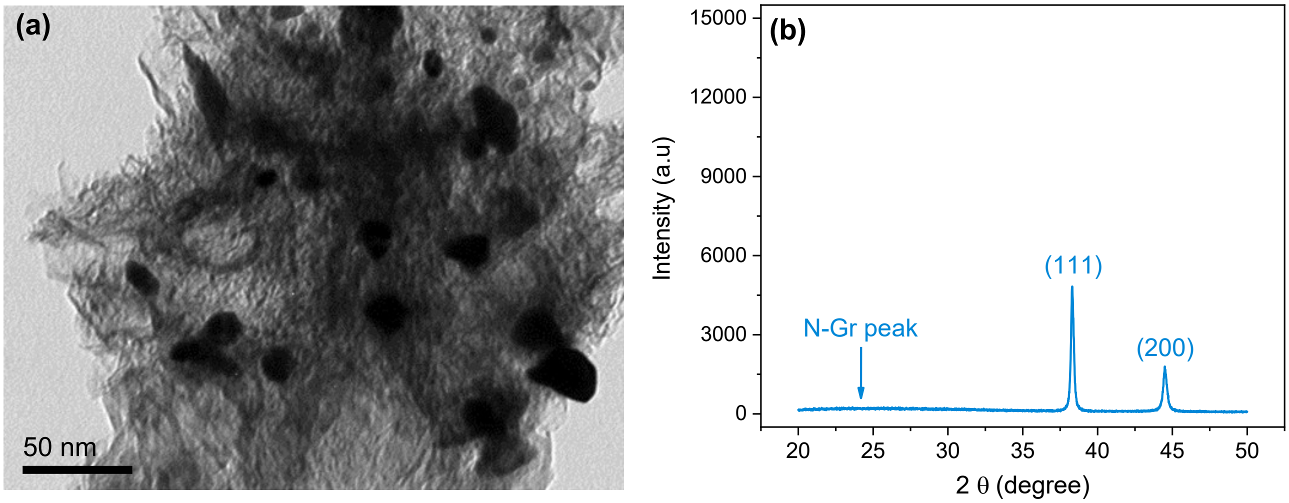

Fig. S3 (a) TEM observation and (b) XRD pattern measurement of as-pyrolyzed Au NPs/N-Gr nanocomposites.

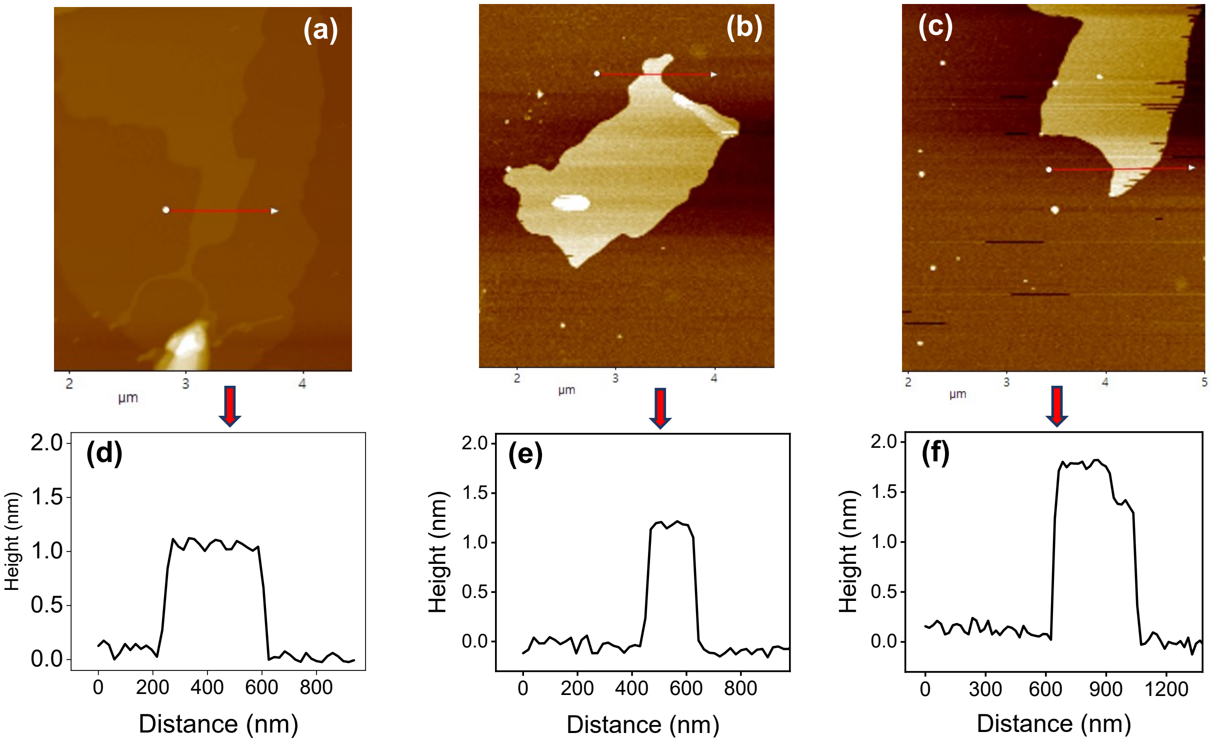

Fig. S4 (a-c) AFM images and (d-f) corresponding height profiles for free graphene, free N-Gr, and Au NCs/N-Gr samples.

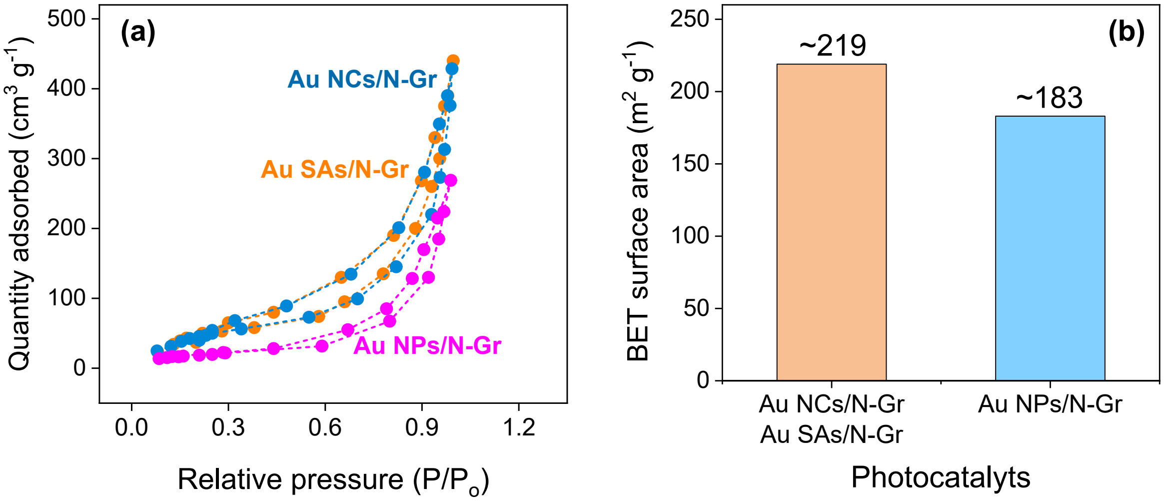

Fig. S5 (a, b) Nitrogen adsorption and desorption isotherms for as-pyrolyzed Au SAs/N-Gr, Au NCs/N-Gr and Au NPs/N-Gr nanocomposites and corresponding BET surface areas.

As can be seen in **Fig. S5a**, the Au SAs/N-Gr and Au NCs/N-gr materials have high abilities to adsorb and desorb nitrogen gas with respect to Au NPs/N-Gr. Therefore, they have a larger surface area of 219 m^2 g^{-1} (**Fig. S5b**).

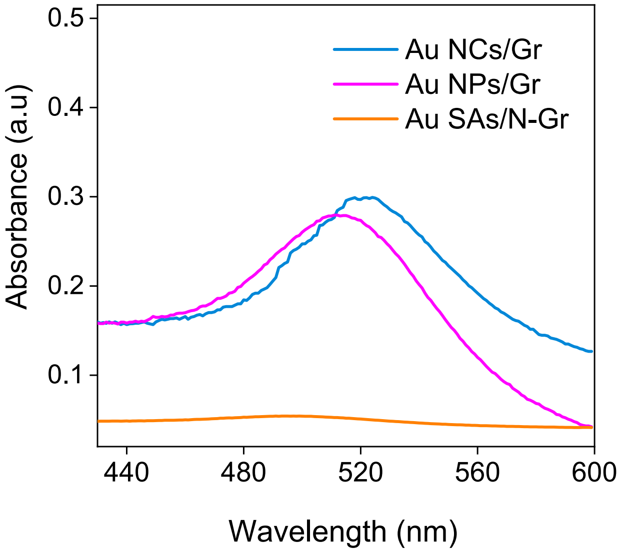

Fig. S6 Change in plasmonic peak position for free Au NPs, Au NPs/N-Gr, and Au NCs/N-Gr nanocomposites surrounded by water medium measured by UV-vis spectroscopy.

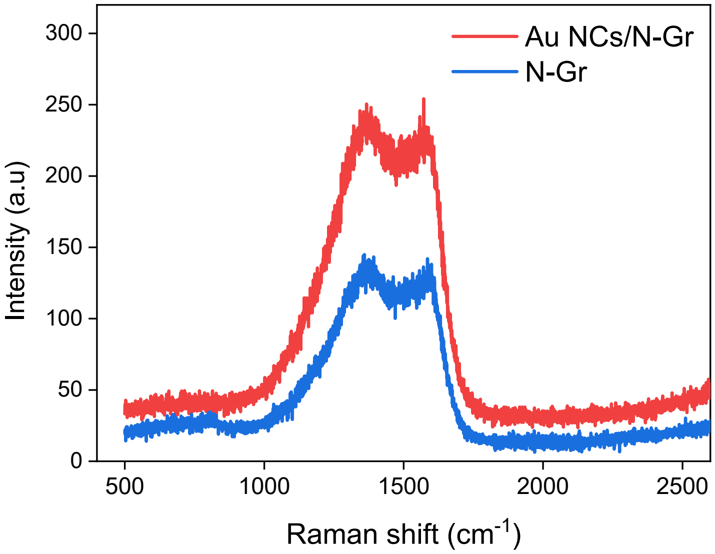

Fig. S7 Raman signal enhancement of N-Gr and Au NCs/N-Gr samples.

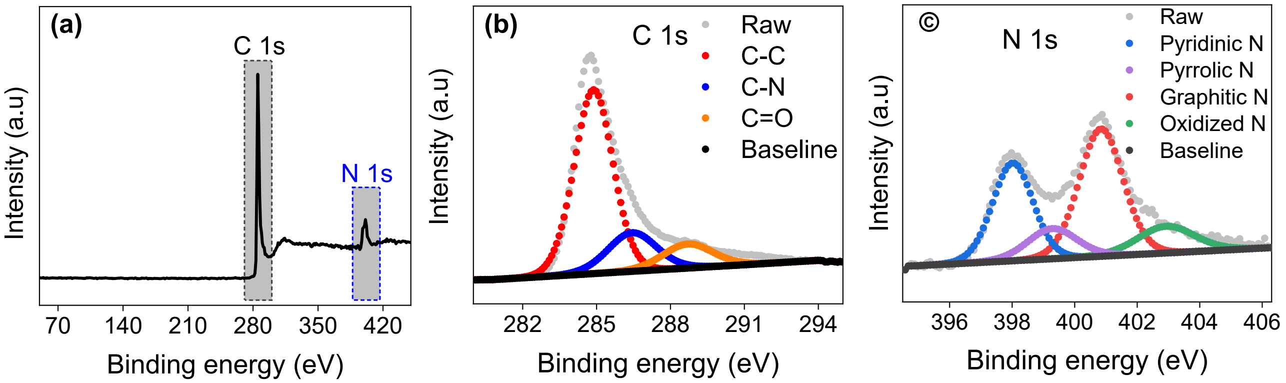

Fig. S8 (a-c) XPS analysis for as-pyrolyzed free N-Gr.

The chemical composition of N-Gr-related materials is examined by XPS measurement in **Fig. S8a**, in which the atomic content of the N dopant is 3.42 at%.

As shown in **Fig. S8b**, the C 1s XPS spectra indicate the different bonding states for C atoms present in the N-Gr support. The main contribution observed at 284.89 eV relates to graphite-like C-C bonds, the other located at 286.45 eV is characteristic of C-N bonds, and the peak at 288.86 eV is assigned to the contribution of C=O bonds from the oxygen adsorption.

In this case, the high-resolution XPS of the N 1s is fitted into four peaks, as shown in **Fig. S8c**. The peak found at 398.04 eV corresponds to the pyridinic-N species, the second one at 399.33 eV belongs to pyrrolic-N components, the other at 400.87 eV relates to graphitic-N bonds, and the last located at 402.90 eV is characteristic of oxidized-N species.

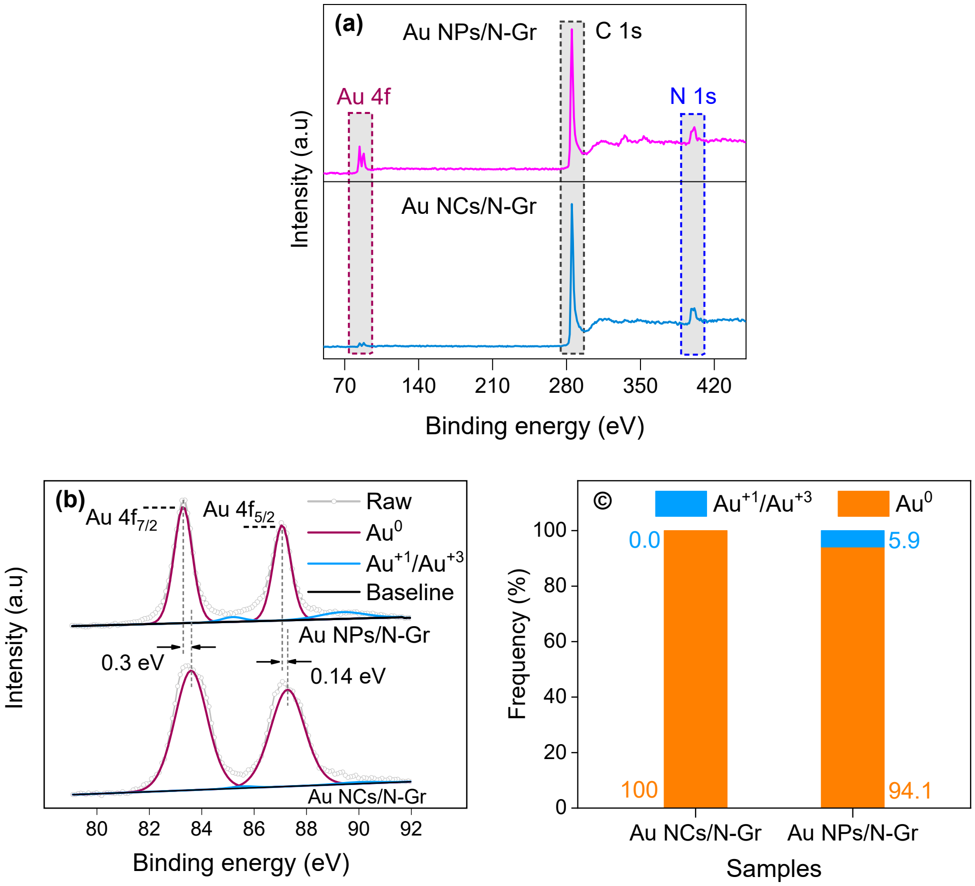

Fig. S9 (a) Full XPS survey measurements for as-pyrolyzed Au NCs/N-Gr and Au NPs/N-Gr nanocomposites. (b) High-resolution XPS analysis for Au 4f. (c) corresponding contribution of Au^0 and Au^{+1}/Au^{+3} to as-prepared Au NCs and Au NPs dispersed into N-Gr support.

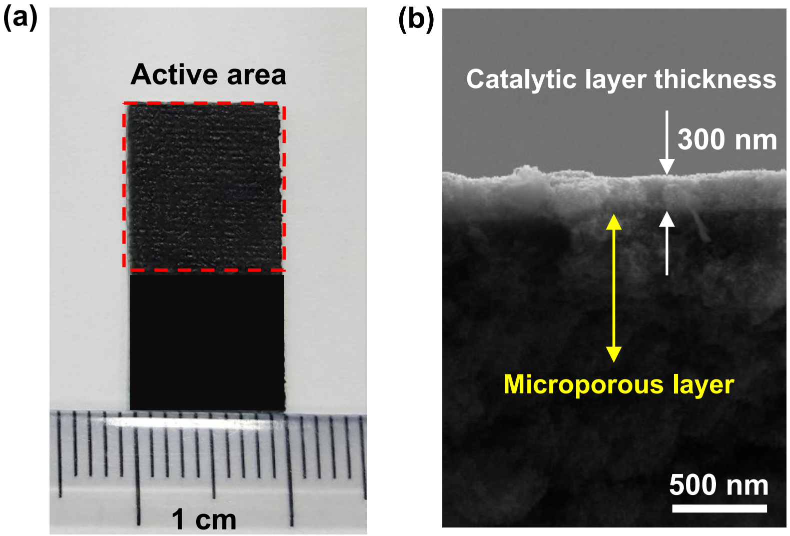

Fig. S10 (a) Photograph of electrode for photoelectrocatalytic purpose. (b) FESEM cross-sectional image for catalytic layer thickness.

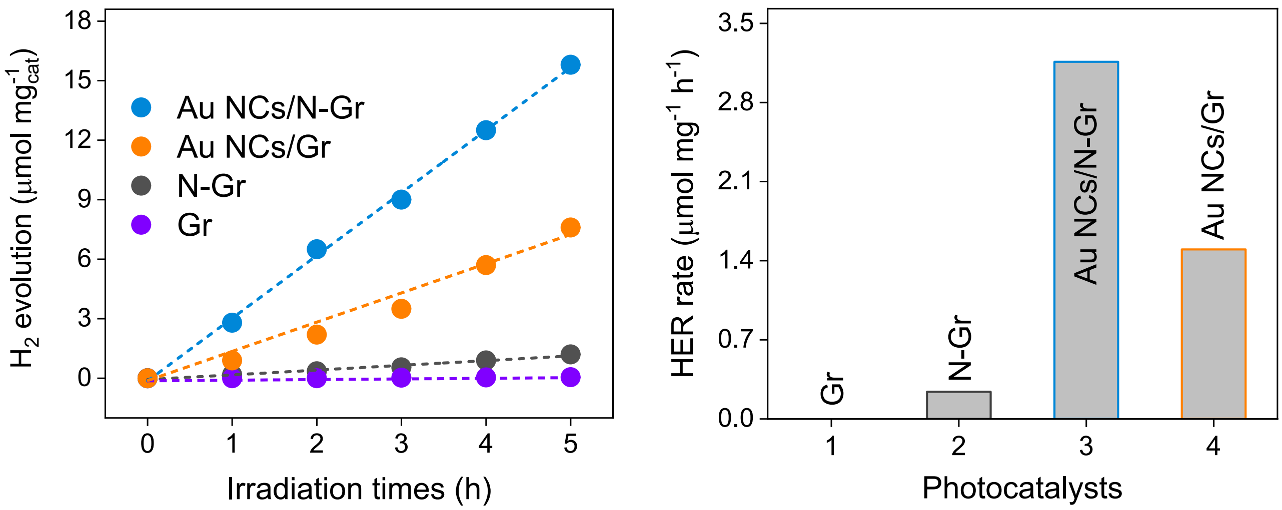

Fig. S11 Room temperature (25 °C) photocatalytic HER performances in a mixed aqueous solution of 0.25 M Na_2SO_3 and 0.25 M Na_2S for Gr, N-Gr, Au NCs/Gr, and Au NCs/N-Gr photocatalysts under the irradiation of visible-light.

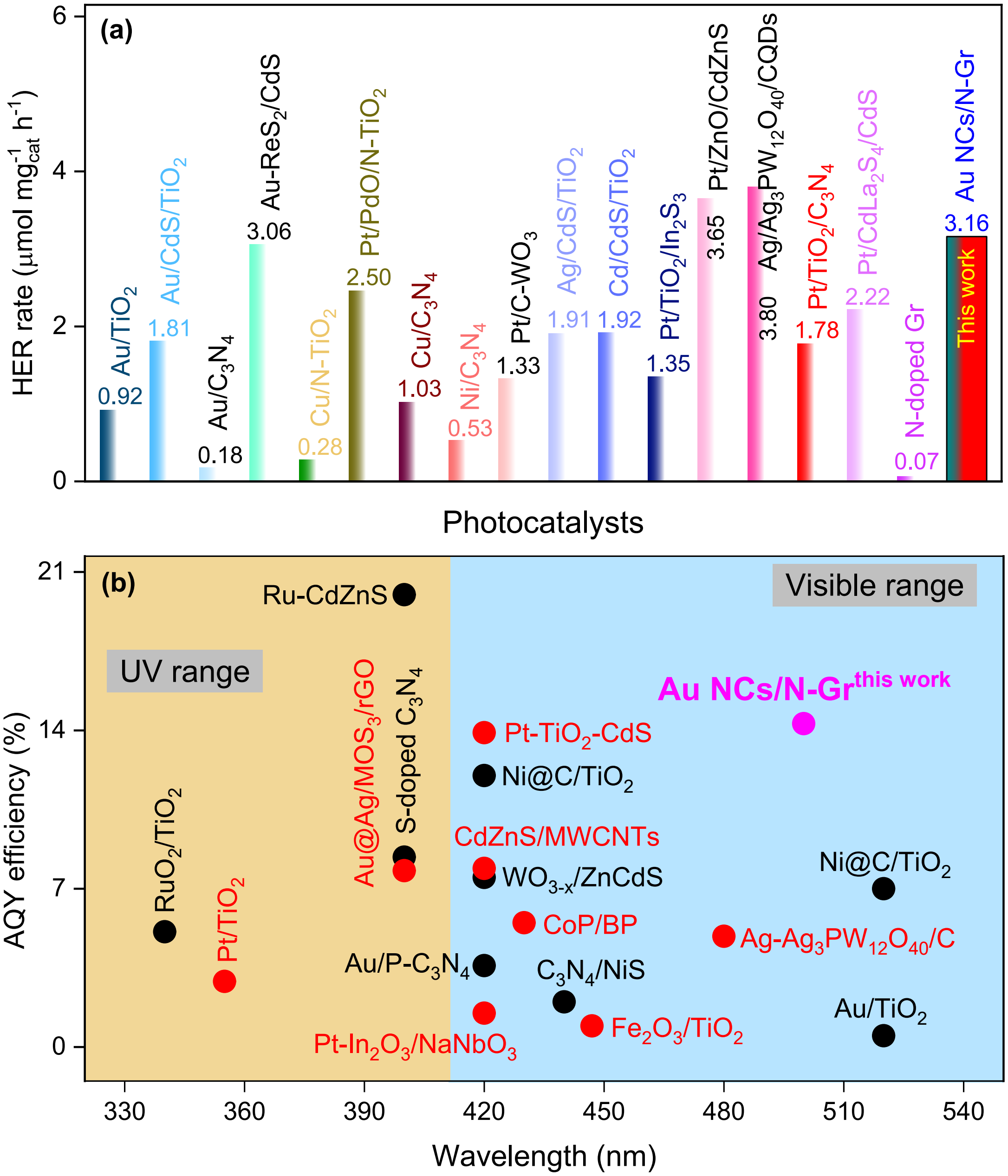

Fig. S12 (a) Comparison of HER rate ($\mu mol\ mg_{cat}^{-1}\ h^{-1}$) based on the different metal-loaded semiconductor hybrid systems under visible-light.[1-17] (b) Comparison of apparent quantum yield (AQY) efficiency based on the different advanced HER photocatalysts.[1, 15, 18-30]

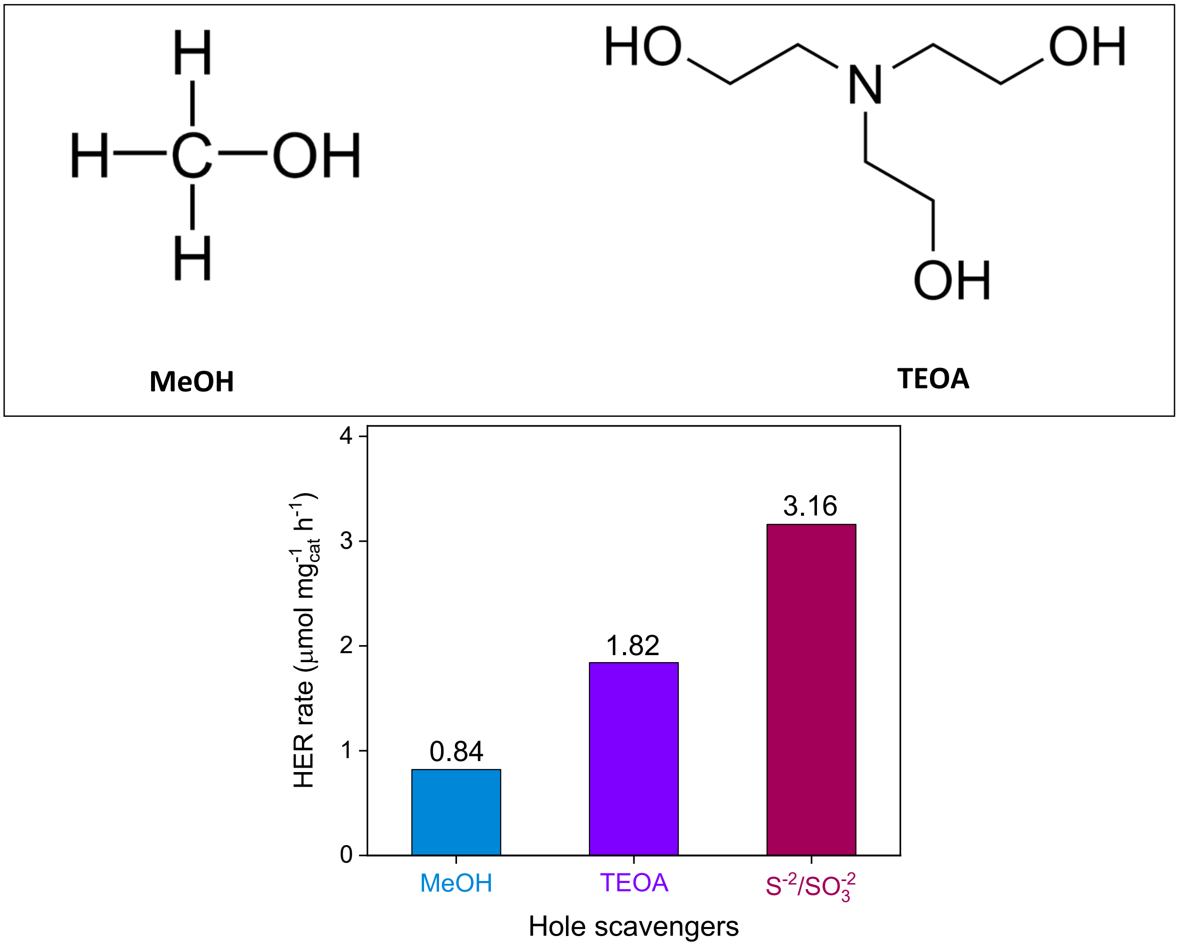

Fig. S13 Photocatalytic hydrogen production rate over Au NCs/N-Gr in different sacrificial hole scavengers: MeOH, TEOA, and Na_2S/Na_2SO_3.

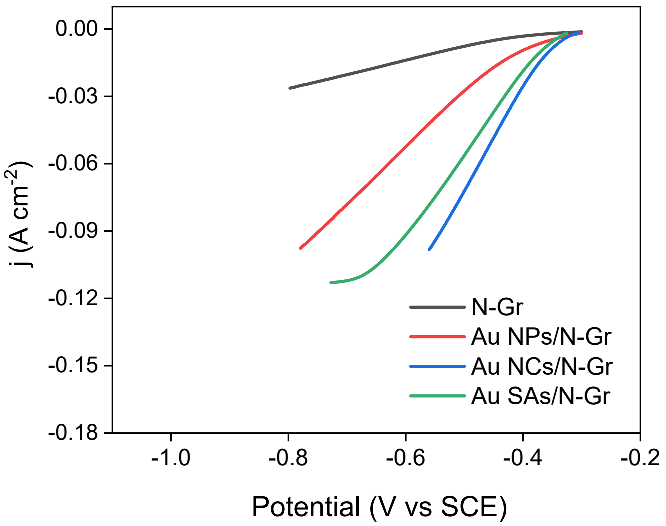

Fig. S14 HER performance over free N-Gr, Au NPs/N-Gr, Au NCs/N-Gr, and Au ASs/N-Gr samples based on LSV responses recorded in in 0.1 M H_2SO_4 electrolyte at a scan value of 20 mV s^{-1}.

FDTD simulations

The intensity distribution of the electric field in the supported Au spherical clusters on N-Gr was numerically investigated by the three-dimensional (3-D) Finite-Difference Time-Domain (FDTD) method. In the numerical simulation, the spatial resolution (grid size) was set to one twentieth of the radius, *r*, for example, 0.5 nm for Au NPs (*r*=10nm), 0.025nm for Au NCs (*r*=0.5nm), and 0.0125 for Au SAs (*r*=0.25nm). And the refractive index of the surrounding material (water) was set to 1.333.

Fig. S15 Built structures for FDTD simulation consisting of Au nanoparticles, Au nanoclusters, and Au single atoms loaded on N-Gr support.

DFT Calculations

a) Computational details

The calculations were performed at the level of Density Functional Theory (DFT), as implemented in VASP 6.1.1 code.[31-33] The valence electrons, C ($2s^2 2p^2$), N ($2s^2 2p^3$), and Au ($6s^1 5d^{10}$) have been expanded on a set of plane waves with a kinetic cut-off of 400 eV, whereas the core electrons were treated with the Projector Augmented Wave (PAW) approach.[34, 35] The Perdew-Burke-Ernzerhof (PBE) exchange−correlation functional was used[36]. The truncation criteria for electronic and ionic loops were set to 10^{-6} eV and -10^{-3} eV/Å, respectively. The reciprocal space has been sampled by a Γ-centered mesh adopting a 5×5×1 grid. The grid was increased to 20×20×1 for the Density Of States (DOS) calculations. Dispersion forces have been considered according to the Grimme's D3 parametrization scheme.[37] A vacuum region ~ 20 A thick was added to every simulation box in order to avoid spurious effects coming from the interaction between periodic replica of the system along the periodic direction.

Different Au-N-graphene models have simulated as follows. We first fully optimized the graphene unit cell, and then we used a 4×4 supercell, containing 32 atoms to model Au atom adsorption on N-graphene. The nitrogen-concentration was 3.1%. Au_{20} on N-Gr was modeled using a large 14×14 supercell in order to accommodate the nanocluster. The number of atoms in the simulation cell was 412. The Nitrogen-dopant concentration was kept similar to that of the previous case (4.1%). The Au(111) surface was modelled from the fully optimized bulk crystal structure of Au, and the atomic coordinates of a five-layers slab have been fully relaxed.

b) N-doped graphene, N-Gr

Table S1 reports the optimized lattice parameters of N-Gr at the PBE level of theory compared with that of Gr. After N-doping graphene, the C-C bond length changes from 1.418 to 1.414 Å. The Fermi level in N-Gr is shifted to the valence band, which confirm that Nitrogen-doped graphene behaves as a n-type semiconductor. After doping with Nitrogen, the geometry remains flat as in pristine graphene.

Table S1. Optimized lattice parameters (*a*, *b*, and *γ*) of graphene (Gr) and N-graphene (N-Gr) at PBE level of theory. Calculated C-C and C-N bond distances are reported too.

	a (Å)	b (Å)	γ (º)	$d_{\text{C-C}}$ (Å)	$d_{\text{C-N}}$ (Å)
Graphene	34.38	34.38	120.00	1.418	---
N-graphene	34.38	34.38	120.00	1.414	1.408

b) Au_{20} gas-phase Nano Clusters

We considered three Au_{20} isomers, a tetrahedral one and two planar structures, **Fig. S16**. The tetrahedral is the most stable isomer as also shown experimentally;[38] in our calculations it is 2.80 eV more stable than the planar isomer b; the planer isomer c is 2.94 eV higher in energy than the tetrahedral one. In the tetrahedral isomer the Au-Au bond lengths span from 2.63 to 2.93 Å while in the planar one they go from 2.64 to 2.85 Å.

Both T-Au_{20} and P-Au_{20} isomers exhibit a band gap: 1.8 eV for T-Au_{20} and 0.69 eV for P-Au_{20}, **Fig. S16**.

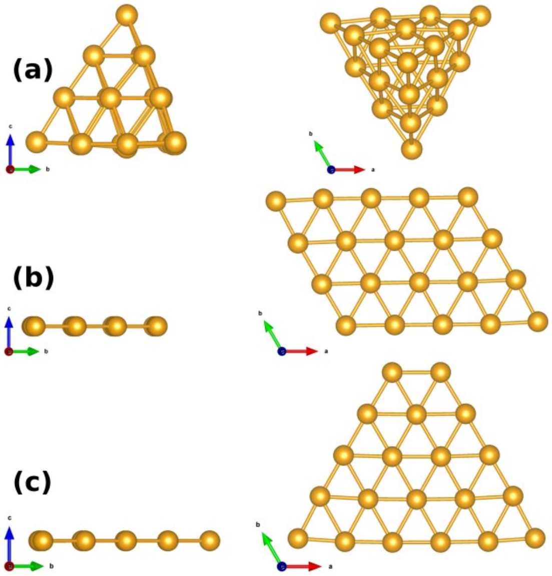

Fig. S16 (a) Side and top view of tetrahedral Au_{20} (T-Au_{20}), (b, c) side and top views of two isomers of planar Au_{20} (P-Au_{20}).

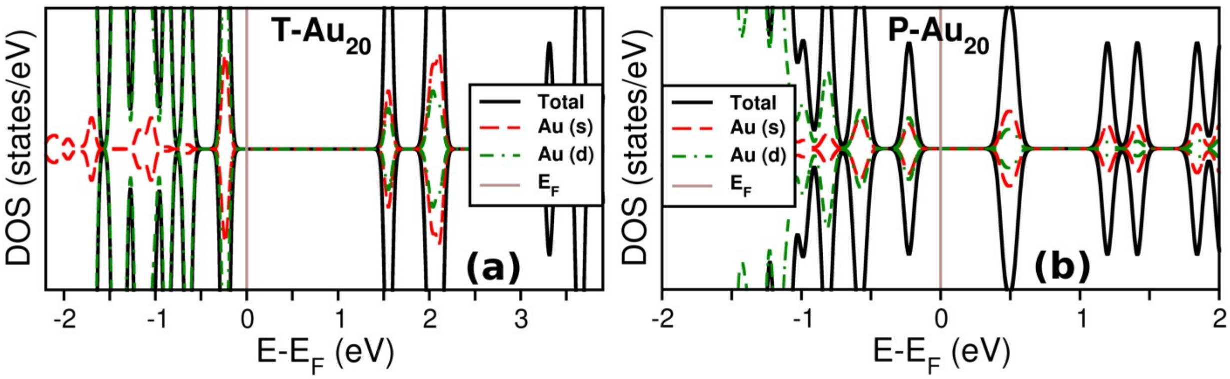

Fig. S17 (a, b) Density of states for the T-Au_{20} and P-Au_{20} gas-phase isomers.

c) Au_1/N-Gr

We considered five adsorption sites to study the Au atom interaction with N-graphene: on top of N (N-top$_1$), on the center of the N-aromatic ring (N-top$_2$); on top of the ortho (C-ortho), meta (C-meta), and para (C-para) C positions of the N-aromatic ring. We computed the binding energy (*BE*) (**Table S2**) as follows:

$$BE = E_{Au-N-Gr} - (E_{N-Gr} + E_{Au})$$

Table S2. Binding energy (in eV), bond lengths (in Å), total charge transfer (*CT*) from N-Gr to Au (in *e*), atomic magnetic magnetization (*MM*) contribution due to Au *s* orbital, and total dipole moment (μ) of the system.

site	*BE* (eV)	*d* C-N	*d* Au-N	*d* Au-C	*CT* (e)	*MM* Au (s)	μ (a.u)
N-top$_1$	-0.66	1.410	3.161	---	-0.344	0.24	1.38
N-top$_2$	-0.68	1.408, 1.411	3.244	---	-0.340	0.22	1.33
C-ortho	-0.99	1.405, 1.459	---	2.189	-0.194	0.00	0.68
C-meta	-0.68	1.395, 1.420	---	2.318	-0.249	0.00	0.92
C-para	-0.82	1.411, 1.420	---	2.224	-0.243	0.00	0.75

In the most favorable adsorption site Au is on top of the C-ortho position with a bond length of 2.189 Å and an adsorption energy of -0.99 eV. The magnetic moment of Au is zero. The bonding of Au on top of N is weaker, -0.68 eV, and there is a residual magnetic moment on Au, indicating a different binding mode. This is further supported by the much longer optimal Au-N distance, 3.24 Å, than for adsorption on top of C, **Table S2**. The different magnetic moment found on Au when the atom is adsorbed on top of C or on top of N is indicative of a different bonding nature. The coupling of the 6s electron of Au with the unpaired electrons introduced in the structure by N-doping can lead to a covalent-polar Au-surface bond, with partial charge transfer towards the Au atom, a very electronegative species. **Fig. S18** shows the side and top views of the optimized structure of Au on top of N on N-graphene and the DOS curves. From the DOS plot one can see that the Au 6s orbital has the majority spin component full, and the minority spin component crossed by the Fermi level, which indicates a Au atom with partial negative character.

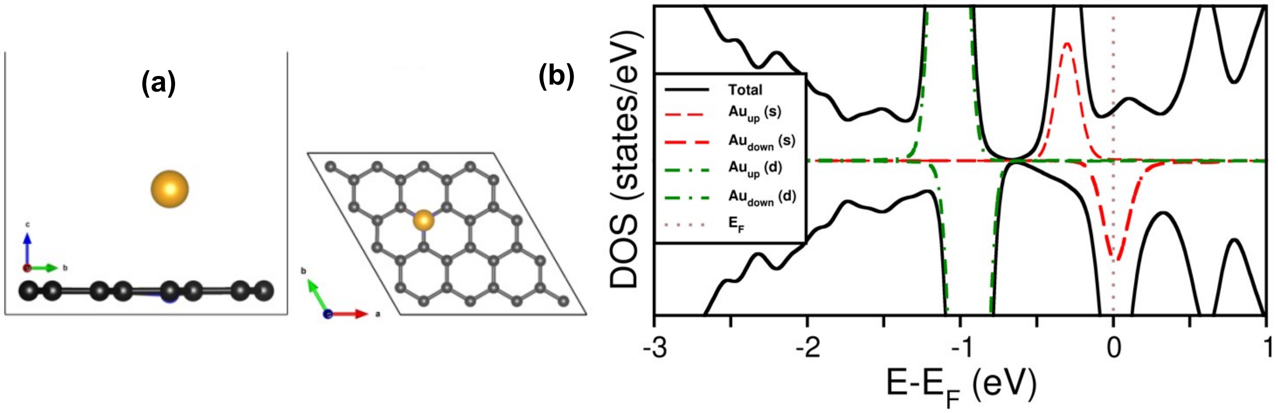

Fig. S18 Optimized structure and density of states of Au adsorbed on top of N on N-Gr (Ntop$_1$): left: (a, b) side and top views; right: the density of states. Black, blue and yellow balls represent the carbon, nitrogen and gold atoms. In the DOS the red, green line, and black lines correspond to the Au *s*, and *d* orbitals and the total DOS, respectively.

Fig. S19 shows the same properties for a Au atom adsorbed on top of C (C-para case). Here the Au *6s* orbital is completely full, both majority and minority spin components are below the Fermi level. There is no spin polarization on Au, which has a 6s^2-type configuration and a Au^{-1} charged state. Notice that the same electronic structure is found for all the C-cases, C-ortho, C-meta, and C-para.

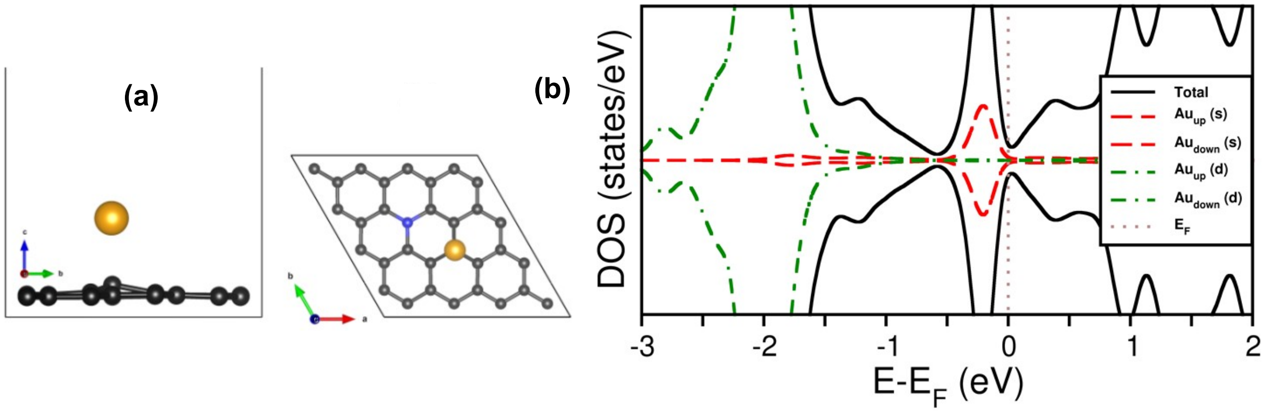

Fig. S19 Optimized structure and density of states of Au adsorption on C-top of N-Gr: left: (a, b) side and top views; right: the density of states. Black, blue and yellow balls represent the carbon, nitrogen and gold atoms. In the DOS the red, green line, and black lines correspond to the Au *s*, and *d* orbitals and the total DOS, respectively.

To further characterize the bonding nature and confirm the change in configuration of the Au atoms as one moves it from the N-top site (neutral) to the C-carbon site (negatively charged) we have analyzed the dipole moment curve for the displacement of the Au atom normal to the adsorption site. This property in fact provides a strong proof of the charged nature of an adsorbate.[39] We have constructed the dipole moment curve and the binding energy curve for normal displacements of the Au atom for the N-top and C-para adsorption cases. We started from the optimized geometries (at PBE level) and we computed the properties around the minimum region of the Au-N and Au-C sites, respectively, **Fig. S20a** (potential energy curve) and **Fig. S20b** (dipole moment curve). From **Fig. S20a** we clearly see that the Au-C and Au-N atoms have quite different equilibrium bond distances, and the Au-C bond is stronger that the Au-N one. Moreover, the Au-C bonding is characterized by a strong Au^{-1} character of the metal atom, when compared to the Au-N bond, as can be evinced from the slopes of the curves reported in **Fig. S20b**. This result corroborates what found by the atomic magnetization and DOS analysis.

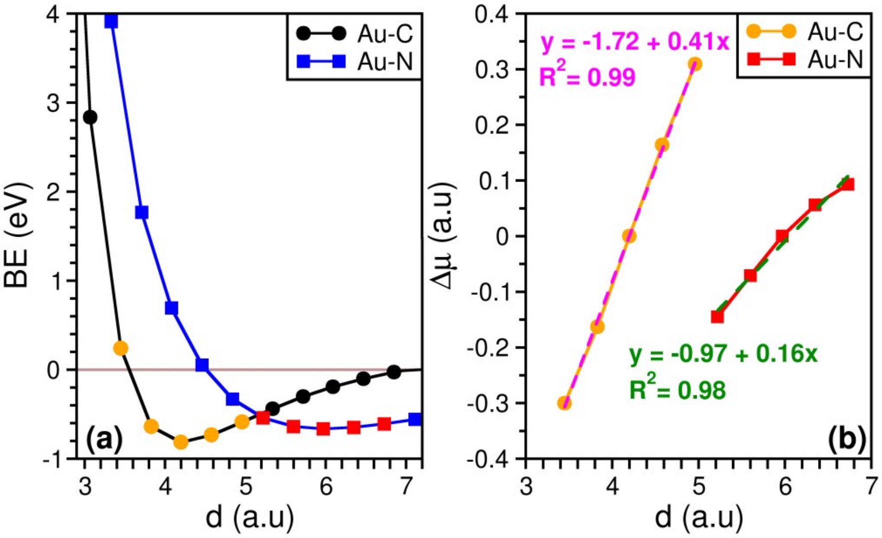

Fig. S20 (a, b) Potential energy and dipole moment curves vs the bond length for adsorption of a single Au atom on the N-top and C-top (para) sites of N-Gr. In (a) the points used to compute the slope of the dipole moment curve are in yellow (C-top) and red (N-top) colors.

d) Au_{20}/Gr and Au_{20}/N-Gr

T-Au_{20} and P-Au_{20} have been adsorbed both on graphene, **Fig. S21** and **S22**, and N-graphene, **Fig. S23** and **S24**. The binding energy (BE) is computed as:

$BE = E_{T\text{-}Au20@N\text{-}Gr} - (E_{N\text{-}Gr} + E_{T\text{-}Au20})$

The results are summarized in **Table S3**.

Table S3. Au_{20} on graphene and N-graphene. Binding energy with (BE_{WD}) and without dispersion (BE_{WOD}) (in eV), relative energy with and without dispersion contribution (RE_{WD} and RE_{WOD}) (in eV), bond lengths (in Å), and dipole moment (in a.u.).

site	BE_{WD}	RE_{WD}	BE_{WOD}	RE_{WOD}	$d_{C\text{-}N}$ (Å)	$d_{Au\text{-}N}$ (Å)	$d_{Au\text{-}C}$ (Å)	μ (a.u)
T-Au_{20}/Gr	-2.26	0.00	0.22	0.00	---	---	3.12-3.46	1.51
P-Au_{20}/Gr	-3.85	1.22	0.45	1.75	---	---	3.32-3.60	1.20
T-Au_{20}/N-Gr	-2.21	0.13	0.30	0.00	1.406	3.48-3.69	3.16-3.52	3.49
P-Au_{20}/N-Gr	-5.14	0.00	-1.04	0.34	1.405	3.50-3.60	3.35-3.66	6.98

On graphene the T-Au_{20} cluster is the ground state, and it is 1.22 eV more stable than the P-Au_{20} isomer. This is smaller than the difference in stability of the two isomers in gas-phase, 2.80 eV. The reason is that now Au_{20} interacts with the surface, and the interface bonding is stronger for the planar cluster which has more atoms in contact with graphene. In fact, the adsorption energy of P-Au_{20} is -3.85 eV, compared to -2.26 eV for T-Au_{20}. This bonding is almost entirely due to dispersion interactions (**Table S3**).

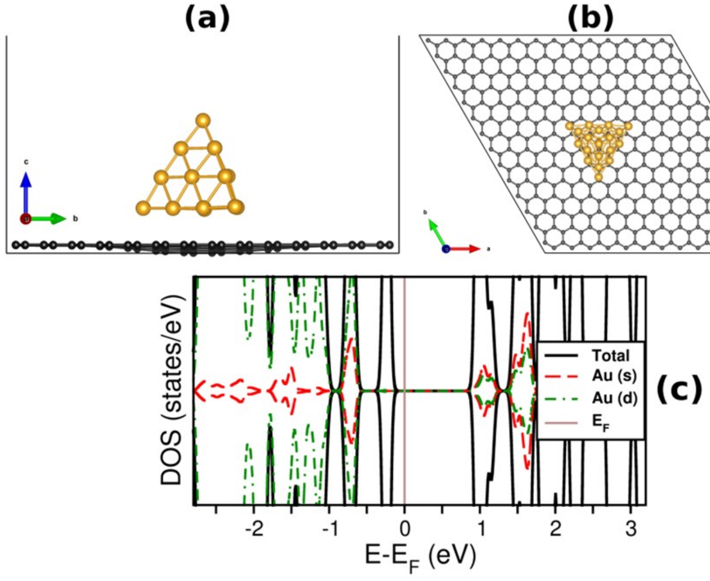

Fig. S21 Optimized structure and density of states of T-Au_{20}/Gr: (a, b) side and top view, and (c) density of states. Black, blue and yellow spheres represent carbon, nitrogen and gold atoms, respectively. The red, green line, and black lines correspond to the Au *s,* Au *d* orbitals and the total DOS, respectively.

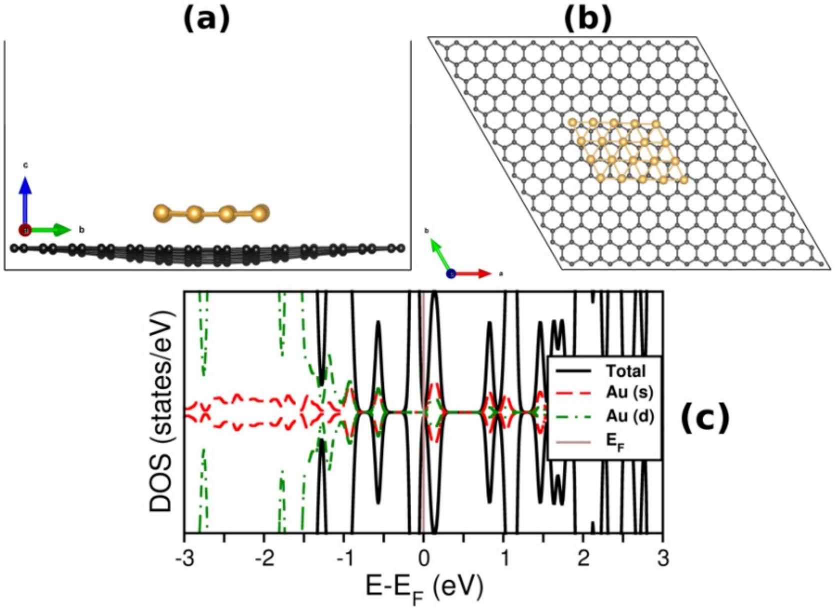

Fig. S22 Optimized structure and density of states of P-Au_{20}/Gr: (a, b) side and top view, and (c) density of states. Black, blue and yellow spheres represent carbon, nitrogen and gold atoms, respectively. The red, green line, and black lines correspond to the Au *s*, Au *d* orbitals and the total DOS, respectively.

The picture is very different on N-graphene. Here, P-Au$_{20}$ becomes the preferred structure, 0.13 eV more stable than the T-Au$_{20}$ isomer. The two structures are thus almost iso-energetic on N-graphene. A similar result has been reported recently in the literature.[40] The bonding, however, is no longer due exclusively to dispersion interactions. In fact, when dispersion contributions are removed, T-Au$_{20}$ is unbound by 0.30 eV while P-Au$_{20}$ is bound by -1.04 eV. This is a genuine chemical bond reflecting the occurrence of an electron transfer at the interface. T-Au$_{20}$ has the same BE on both graphene and N-graphene (0.05 eV more stable on graphene) why P-Au$_{20}$ is by far more stable on N-graphene.

When T-Au$_{20}$ is adsorbed on N-graphene the band gap is reduced by ~0.3 eV with respect to free T-Au$_{20}$ nano-cluster. The empty states of T-Au$_{20}$ are above the Fermi level, indicating the absence of an important charge transfer, **Fig. S23**. For P-Au$_{20}$ on N-graphene the DOS curves show that the empty states of P-Au$_{20}$ are crossed by the Fermi level, indicating the occurrence of a charge transfer from N-graphene to P-Au$_{20}$ which becomes partly negatively charged, **Fig. S24**. This is supported also by the atomic charges of the Au atoms of P-Au$_{20}$, which are considerably more negative on N-graphene (total charge -1.69 e) than on pristine graphene (total charge -0.04 e). This implies a change in the nature of Au$_{20}$, from semiconductor on graphene, to metallic on N-graphene.

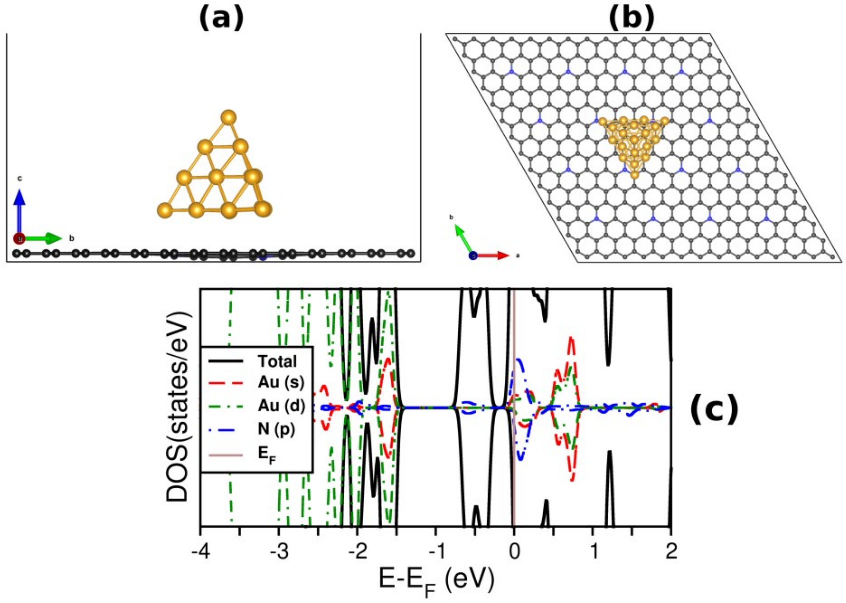

Fig. S23 Optimized structure and density of states of T-Au$_{20}$/N-Gr: (a, b) side and top view, and (c) density of states. Black, blue and yellow balls represent carbon, nitrogen and gold atoms, respectively. The red, green line, and black lines correspond to the Au *s* and Au *d* orbitals and the total DOS, respectively.

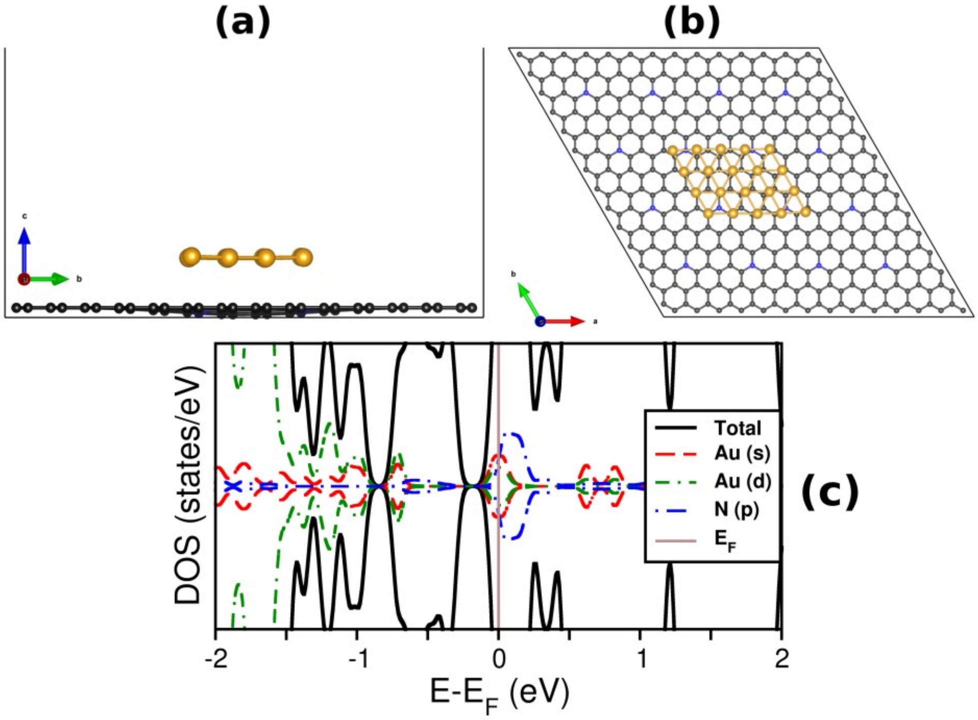

Fig. S24 Optimized structure and density of states of P-Au_{20}/N-Gr: (a, b) side and top view, and (c) density of states. Black, blue and yellow balls represent carbon, nitrogen and gold atoms, respectively. The red, green line, and black lines correspond to the Au *s* and Au *d* orbitals and the total DOS, respectively.

e) H adsorption on N-Gr

Adsorption of atomic hydrogen on a C and N atoms of N-graphene has been studied. The adsorption energy is defined with respect to the H_2 molecule, so that a positive ΔE_H value indicates an endothermic process. H_2 dissociation on N-graphene is thermodynamically unfavorable. The most strongly binding site is a C atom in ortho position, **Table S4** and **Fig. S25**.

Table S4. Adsorption energy of H on N-Gr (in eV) and bond lengths between N-H and C-H (in Å). ΔE_H is given with respect to the ½ H_2. The most stable scenario is indicated in shading color.

site	ΔE_H	$d_{N\text{-}H}$	$d_{C\text{-}H}$
N	1.62	1.05	---
C_{ortho}	0.41	---	1.12
C_{meta}	1.01	---	1.13
C_{para}	0.66	---	1.12

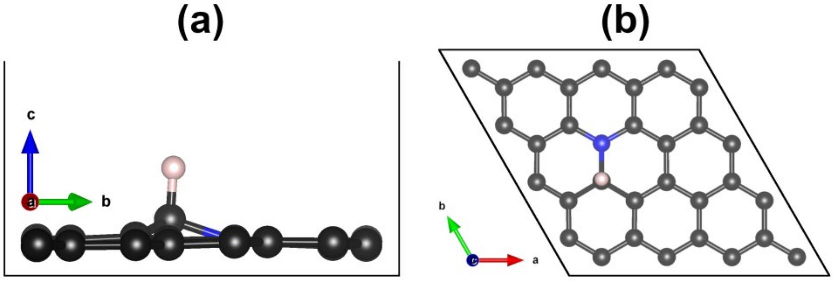

Fig. S25 (a, b) Side and top views of the most stable adsorption site of H on N-Gr. Black, blue and white spheres represent the carbon, nitrogen and hydrogen atoms, respectively.

f) H adsorption on Au_1/N-Gr (Au on top of C_{ortho})

H adsorption on Au_1/N-graphene results into an adsorption energy of -0.60 eV, **Table S5** and **Fig. S26**. Therefore, H_2 dissociation on N-graphene is thermodynamically favorable. The Au atom is sitting on the most stable adsorption site, the C atom in ortho position to the N atom of the ring. When H adsorption on a Au atom sitting on C_{meta} or C_{para} positions is considered, the Au atom moves to the C_{ortho} site.

Table S5. Adsorption energy of H on Au_1/N-Gr (in eV) and bond lengths between C-Au, Au-H and C-H (in Å). ΔE_H is given with respect to the ½ H_2. The most stable case is indicated in shading color.

site		ΔE_H	$d_{C\text{-}Au}$	$d_{Au\text{-}H}$
Au	C_{ortho}	-0.60	2.43	1.57

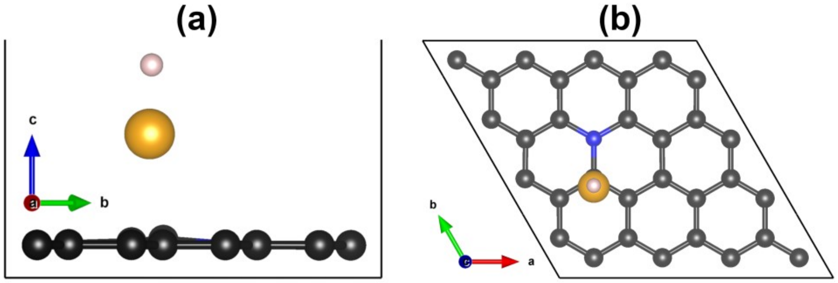

Fig. S26 (a, b) Side and top view of the adsorption of H on Au_1/N-Gr. Black, blue, yellow and white balls represent the carbon, nitrogen, gold, and hydrogen atoms, respectively

g) H adsorption on Au(111)

We considered the H atom adsorption on two sites of Au(111) surface, on top of Au and in the hollow site, **Table S6** and **Fig. S27**. Hydrogen adsorption on this metal surface is endothermic, and the most stable site is the hollow site with ΔE_H = 0.26 eV.

Table S6. Adsorption energy (eV) and Au-H bond distance (Å) of H on Au(111). ΔE_H is given with respect to the ½ H_2. The most stable case is indicated in shading color.

case	ΔE_H	$d_{Au\text{-}H}$
Au1	0.45	1.60
Au23	0.45	1.60
Hollow	0.26	1.93

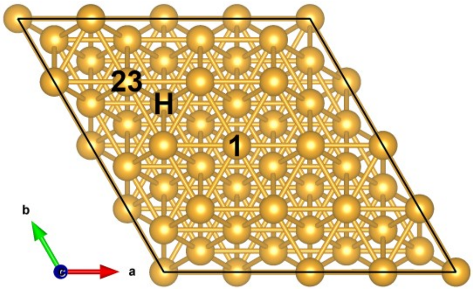

Fig. S27 Hydrogen adsorption sites on Au (111) surface. Yellow spheres represent gold atoms. 1 and 23 sites are two equivalent sites Au, H is a hollow site.

h) H adsorption on T-Au_{20}/Gr, T-Au_{20}/N-Gr, P-Au_{20}/N-Gr

We considered the adsorption properties of an H atom on a T-Au_{20} cluster supported on graphene, **Table S7** and **Fig. S28**. Various sites have been considered, but they all exhibit positive adsorption energies. The most stable adsorption site is on-top of the Au atom at the apical position of the cluster, and in contact with the graphene support with a ΔE_H = 0.45 eV.

Table S7. Adsorption energy of H on T-Au_{20}/Gr (in eV) and bond lengths between C-Au and Au-H (in Å). ΔE_H is given with respect to the ½ H_2. The most stable case is indicated in shading color.

	ΔE_H	$d_{C\text{-}Au}$	$d_{Au\text{-}H}$
Au1	0.45	3.14-3.44	1.61
Au2	0.48	3.20-3.45	1.61
Au6	0.66	3.21-3.46	1.72
Au8	0.60	3.17-3.47	1.61
Au9	0.45	3.18-3.48	1.61
Au11	0.49	3.19-3.43	1.79
Au18	0.47	3.16-3.42	1.80
Au20	0.59	3.16-3.46	1.61

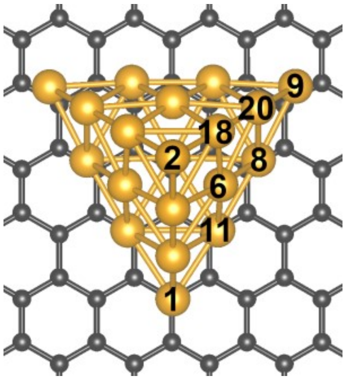

Fig. S28 H adsorption sites on T-Au_{20}/Gr. Black and yellow spheres represent the carbon, and gold atoms, respectively.

The situation is completely different when H adsorption on T-Au_{20}/N-Gr is considered, **Table S8** and **Fig. S29**. In general, the H adsorption is much more favorable on all sites of the T-Au_{20} cluster, with the most favorable site corresponding to the apical Au_1 atom where ΔE_H = -0.40 eV. The H adsorption from endothermic on T-Au_{20}/Gr becomes exothermic on T-Au_{20}/N-Gr. This is due to the charge transfer from the support to the Au nano cluster, which occurs only on N-doped graphene.

Table S8. Adsorption energy of H on T-Au_{20}/N-Gr (in eV) and bond lengths between C-Au, N-Au and Au-H (in Å). ΔE_H is given with respect to the ½ H_2. The most stable case is indicated in gray color.

	ΔE_H	$d_{C\text{-}Au}$	$d_{N\text{-}Au}$	$d_{Au\text{-}H}$
Au1	-0.40	3.37-3.50	3.48-3.49	1.63
Au2	0.09	3.17-3.50	3.46-3.56	1.63
Au3	-0.15	3.31-3.52	3.46-3.56	1.62
Au7	0.22	3.31-3.51	3.38-3.53	1.60
Au8	0.10	3.31-3.50	3.40-3.47	1.63
Au9	-0.39	3.29-3.54	3.42-3.50	1.63
Au18	0.17	3.21-3.50	3.57-3.59	1.77
Au19	0.13	3.27-3.53	3.46-3.59	1.77

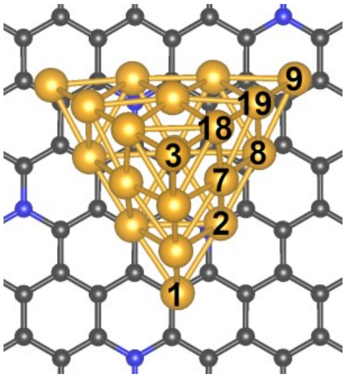

Fig. S29 H adsorption sites on T-Au_{20}/N-Gr. Black, blue and yellow balls represent carbon, nitrogen and gold atoms, respectively.

The same effect due to the charge transfer from N-graphene is found when H adsorption on the P-Au_{20}/N-graphene isomer is considered, **Table S9** and **Fig. S30**. Also in this case, the strongest adsorption is found for H bound to the Au atoms at the cluster periphery, see Au20 in **Fig. S30**. Here ΔE_H is even more negative than on T-Au_{20}, -0.47 eV.

Table S9. Adsorption energy of H on P-Au_{20}/N-Gr (in eV) and bond lengths between C-Au, N-Au and Au-H (in Å). ΔE_H is given with respect to the ½ H_2. The most stable case is indicated in shading color.

	ΔE_H	$d_{C\text{-}Au}$	$d_{N\text{-}Au}$	$d_{Au\text{-}H}$
Au7	-0.20	3.39-3.60	3.51-3.63	1.61
Au14	0.23	3.31-3.54	3.42-3.61	1.79
Au20	-0.47	3.40-3.58	3.52-3.64	3.72

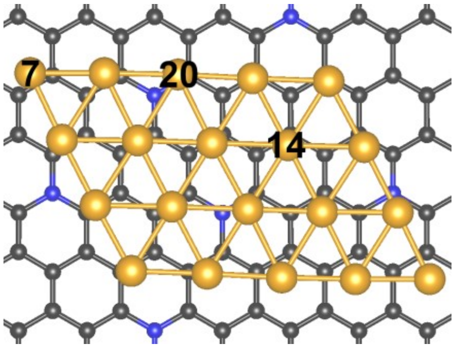

Fig. S30 H adsorption sites on P-Au_{20}/N-Gr. Black, blue and yellow spheres represent the carbon, nitrogen and gold atoms, respectively.

i) HER of various catalysts examined

Table S10. Computed free energy for the most stable cases of H adsorbed on different supports.

Name	Catalyst	ΔE_H (eV)	ΔE_{ZPE} (eV)	$T\Delta S_H$ (eV)	ΔG_{H^*} (eV)
N-Gr	N-Gr	0.41	0.18	-0.19	0.78
Au(111)	Au NPs	0.26	-0.01	-0.19	0.44
T-Au_{20}/N-Gr	Au NC	-0.40	-0.01	-0.19	-0.22
P-Au_{20}/N-Gr	Au NC	-0.47	-0.01	-0.19	-0.29
Au_1/N-Gr	Au SAs	-0.60	0.03	-0.19	-0.38

j) Work function of N-Gr, Au SAs, Au NCs, and Au NPs

The work function (Φ) of each model was calculated from the optimized structures and using the following equation, where E^{vac} is the vacuum level and ϵ_F is the Fermi energy.

$$\Phi = E^{vac} - \epsilon_F$$

Results are reported in **Table S11**. The calculated work function of the Au(111) surface compares well with the reported experimental value.

Table S11. Calculated work function of N-Gr, Au SAs, Au NCs, and Au NPs catalyst.

Catalyst	Model	Φ / eV
N-Gr	N-Gr	3.54
Au SAs	Au_1	5.84
Au NCs	T-Au_{20}	5.43
	P-Au_{20}	5.34
Au NPs	Au(111)	5.00
Exp [a]		5.10

Ref [a] , H. B. Michaelson, J. Appl. Phys., 1977, 48, 4729.

References

1 O. Elbanna, S. Kim, M. Fujitsuka and T. Majima, *Nano Energy*, 2017, **35**, 1-8.

2 H. Zhao, M. Wu, J. Liu, Z. Deng, Y. Li and B.-L. Su, *Appl. Catal. B: Environ.*, 2016, **184**, 182-190.

3 S. Samanta, S. Martha and K. Parida, *ChemCatChem*, 2014, **6**, 1453-1462.

4 J. Liu, K. Chen, G.-M. Pan, Z.-J. Luo, Y. Xie, Y.-Y. Li, Y.-J. Lin, Z.-H. Hao, L. Zhou, S.-J. Ding and Q.-Q. Wang, *Nanoscale*, 2018, **10**, 19586-19594.

5 H.-y. Lin and C.-y. Shih, *J. Mol. Catal. A: Chem.*, 2016, **411**, 128-137.

6 I. Chiu, S.-X. Lin, C.-T. Kao and R.-J. Wu, *Inter. J. Hydrogen Energ.*, 2014, **39**, 14574-14580.

7 M. Fan, C. Song, T. Chen, X. Yan, D. Xu, W. Gu, W. Shi and L. Xiao, *RSC Adv.*, 2016, **6**, 34633-34640.

8 M. Ou, S. Wan, Q. Zhong, S. Zhang and Y. Wang, *Inter. J. Hydrogen Energ.*, 2017, **42**, 27043-27054.

9 C. Sun, H. Zhang, H. Liu, X. Zheng, W. Zou, L. Dong and L. Qi, *Appl. Catal. B: Environ.*, 2018, **235**, 66-74.

10 P. Yang, J. Zhao, J. Wang, B. Cao, L. Li and Z. Zhu, *J. Mater. Chem. A*, 2015, **3**, 8256-8259.

11 W. Zhao, J. Liu, Z. Deng, J. Zhang, Z. Ding and Y. Fang, *Inter. J. Hydrogen Energ.*, 2018, **43**, 18232-18241.

12 X. Wang, G. Liu, L. Wang, Z. G. Chen, G. Q. Lu and H. M. Cheng, *Adv. Energy Mater.*, 2012, **2**, 42-46.

13 B. Chai, T. Peng, P. Zeng and J. Mao, *J. Mater. Chem.*, 2011, **21**, 14587-14593.

14 S. R. Lingampalli, U. K. Gautam and C. N. R. Rao, *Energy Environ. Sci.*, 2013, **6**, 3589-3594.

15 J. Liu, H. Zhang, D. Tang, X. Zhang, L. Yan, Y. Han, H. Huang, Y. Liu and Z. Kang, *ChemCatChem*, 2014, **6**, 2634-2641.

16 B. Chai, T. Peng, J. Mao, K. Li and L. Zan, *Phys. Chem. Chem. Phys.*, 2012, **14**, 16745-16752.

17 L. K. Putri, B.-J. Ng, W.-J. Ong, H. W. Lee, W. S. Chang and S.-P. Chai, *ACS Appl. Mater. Interfaces*, 2017, **9**, 4558-4569.

18 B. Tian, B. Tian, B. Smith, M. C. Scott, R. Hua, Q. Lei and Y. Tian, *Nat. Commun.*, 2018, **9**, 1397.

19 A. B. Yousaf, M. Imran, S. J. Zaidi and P. Kasak, *Sci. Rep.*, 2017, **7**, 6574.

20 J. Nemoto, N. Gokan, H. Ueno and M. Kaneko, *J. Photochem. Photobiol. A: Chem.*, 2007, **185**, 295-300.

21 H. Lv, Y. Huang, R. T. Koodali, G. Liu, Y. Zeng, Q. Meng and M. Yuan, *ACS Appl. Mater. Interfaces*, 2020, **12**, 12656-12667.

22 T. Chen, Z. Feng, G. Wu, J. Shi, G. Ma, P. Ying and C. Li, *J. Phys. Chem. C*, 2007, **111**, 8005-8014.

23 J. Lv, T. Kako, Z. Li, Z. Zou and J. Ye, *J. Phys. Chem. C*, 2010, **114**, 6157-6162.

24 L. Qi, J. Yu and M. Jaroniec, *Phys. Chem. Chem. Phys.*, 2011, **13**, 8915-8923.

25 X. Wang, W.-c. Peng and X.-y. Li, *Inter. J. Hydrogen Energ.*, 2014, **39**, 13454-13461.

26 P. Zeng, X. Zhang, X. Zhang, B. Chai and T. Peng, *Chem. Phys. Lett.*, 2011, **503**, 262-265.

27 B. Vedhanarayanan, C.-C. Chen and T.-W. Lin, *J. Power Sources*, 2020, **477**, 229033.

28 M. Humayun, Q. Fu, Z. Zheng, H. Li and W. Luo, *Appl. Catal. A: Gen.*, 2018, **568**, 139-147.

29 L. Wang, Z. Yao, F. Jia, B. Chen and Z. Jiang, *Dalton Trans.*, 2013, **42**, 9976-9981.

30 J. Hong, Y. Wang, Y. Wang, W. Zhang and R. Xu, *ChemSusChem*, 2013, **6**, 2263-2268.

31 G. Kresse and J. Furthmüller, *Phys. Rev. B*, 1996, **54**, 11169-11186.

32 G. Kresse and J. Furthmüller, *Comput. Mater. Sci.*, 1996, **6**, 15-50.

33 G. Kresse and J. Hafner, *Phys. Rev. B*, 1993, **47**, 558-561.

34 P. E. Blöchl, *Phys. Rev. B*, 1994, **50**, 17953-17979.

35 G. Kresse and D. Joubert, *Phys. Rev. B*, 1999, **59**, 1758-1775.

36 J. P. Perdew, K. Burke and M. Ernzerhof, *Phys. Rev. Lett.*, 1996, **77**, 3865-3868.

37 S. Grimme, J. Antony, S. Ehrlich and H. Krieg, *J. Chem. Phys.*, 2010, **132**, 154104.

38 J. Li, X. Li, H.-J. Zhai and L.-S. Wang, *Science*, 2003, **299**, 864.

39 P. S. Bagus, G. Pacchioni and M. R. Philpott, *J. Chem. Phys.*, 1989, **90**, 4287-4295.

40 S. S. Yamijala, A. Bandyopadhyay and S. K. Pati, *J. Phys. Chem. C*, 2014, **118**, 17890-17894.